LAWRENCE
LIVERMORE
NATIONAL
LABORATORY

LLNL-JRNL-811691

# Standoff Detection of Chemical Plumes from High Explosive Open Detonations Using Swept-Wavelength External Cavity Quantum Cascade Lasers

M. C. Phillips, S. S. Harilal, J. Yeak, J. Jones, S. Wharton, B. E. Bernacki

June 16, 2020

Journal of Applied Physics

## Disclaimer

# Standoff detection of chemical plumes from high explosive open detonations using a swept-wavelength external cavity quantum cascade laser

**Mark C. Phillips,[1,2] Sivanandan S. Harilal,[3] Jeremy Yeak,[2] R. Jason Jones,[1] Sonia Wharton,[4] Bruce E. Bernacki[3]**

[1]James C. Wyant College of Optical Sciences, University of Arizona, Tucson, AZ 85721 USA

[2]Opticslah, LLC, Albuquerque, NM 87106 USA

[3]Pacific Northwest National Laboratory, 902 Battelle Boulevard, Richland, WA 99352 USA

[4]Lawrence Livermore National Laboratory, Livermore, CA 94550 USA

**Corresponding author: Mark C. Phillips, mphillips@optics.arizona.edu**

## ABSTRACT

A swept-wavelength external cavity quantum cascade laser (ECQCL) is used to perform standoff detection of combustion gases in a plume generated from an outdoor high-explosive (HE) open detonation. The swept-ECQCL system was located at a standoff distance of 830 m from a 41 kg charge of LX-14 (polymer-bonded high explosive) and was used to measure the infrared transmission/absorption through the post-detonation plume as it propagated through the beam path. The swept-ECQCL was operated continuously to record broadband absorption spectra at a 200 Hz rate over a spectral range from 2050-2230 $cm^{-1}$ (4.48-4.88 μm). Fitting of measured spectra was used to determine time-resolved column densities of CO, $CO_2$, $H_2O$, and $N_2O$. Analysis of visible video imagery was used to provide timing correlations and to estimate plume dimensions, from which gas mixing ratios were estimated. Measured emission factors and modified combustion efficiency show good agreement with previously reported values.

Keywords: Laser, explosives, infrared, spectroscopy

## I. INTRODUCTION

Measurement of gas species and their concentrations produced from detonations of high explosives (HE) is important for optimizing explosives performance, validating thermochemical models of detonation and combustion, and understanding short- and long-term effects of released gases on the environment. Detection of toxic gases CO, NO, and $NO_2$ produced from explosions is important for worker safety in mining operations, especially for work in enclosed spaces.[1] Disposal of unwanted explosives and munitions through open burning (OB) or open detonation (OD) produces various gases and particulates, and there is a need to predict and measure the quantities of these species for regulatory purposes.[2-5] Laboratory experiments performed using small quantities of explosives detonated in enclosed chambers is important, especially for research and method development, but these small-scale tests often do not

reproduce the conditions or end-results occurring in larger-scale ODs. Therefore, measurements of larger-scale OD events provide critical testing and validation information not available otherwise.

Quantification of gas concentrations for many trace gas species and particulates produced from HE detonations can be performed by collecting air samples of the post-detonation region followed by laboratory or online analysis. Trace gases are typically analyzed using laboratory-based gas chromatography and/or mass spectrometry (GC/MS).[2-5] $CO_2$ is typically measured using nondispersive infrared sensors (e.g. LI-COR instruments) and CO is typically measured using electrochemical sensors, either on static collected samples or through continuous sampling to measure dynamics (time responses are ~1-10 s for $CO_2$ and ~20-30 s for CO).[2-5]

Sampling of gases produced from HE detonations presents considerable challenges, especially for larger-scale ODs. Personnel and sensitive equipment must be protected from shock and thermal effects, either by enclosing the HE in a blast chamber, or by locating at safe distances from the detonation. For enclosed detonations, gas samples can be obtained directly from the explosive blast chamber making it straightforward to sample uniform and well-mixed product gases and to determine quantitative mixing ratios.[2] However, for ODs the gas plume generated by the HE detonation is unconfined and changes in size and shape as it propagates through the atmosphere. The changing plume volume presents challenges for obtaining representative samples of gases, which may exhibit large variations with time and space. Methods have been developed to use a large-volume inflatable chamber (BangBox) to confine the product gases for OD studies.[5]

For unconfined ODs, point samplers or point sensors located downwind of the detonation may be used to measure gases based on predictions of plume propagation and prevailing winds. However, if wind conditions change from predictions there is a large risk that the point samplers/sensors will not measure the plume. For point sensors located near the ground, there is a risk the plume may loft over the sensor location. The conditions at a single localized point in space may not be representative of general plume conditions and may show large variations in time as the plume propagates past; thus, a fast time response for continuous sensors may be needed to track these plume fluctuations.[6] Point samplers may require precise timing to trigger collection during the plume propagation, and may need to collect multiple samples during the event or else use long collection times. Despite these challenges, point samplers and online sensors have been operated successfully from airborne balloon-based systems to intercept the gas plume downwind from ODs.[3,4]

Optical techniques are a promising method to measure species released from HE detonations in a standoff configuration. Optical emission spectroscopy at ultraviolet, visible, and near-infrared wavelengths has been used to measure temperatures, atomic species, and some molecular species for the hot fireball conditions of the HE.[7-11] Combustion gases $CO_2$, CO, and $H_2O$ have been measured using standoff Fourier Transform Infrared (FTIR) spectroscopy to analyze the mid-wave infrared (MWIR, 3-5 μm) light emitted from HE detonations.[12-16] FTIR emission spectroscopy can be performed at large distances from the source of an OD; for example, remote detection of air-dropped bomb detonations was reported using a standoff distance of 4.8 km.[16] The primary limitation of emission-based optical techniques is that they can only be performed for times when the fireball temperature is high enough to produce emission intensity detectable above the thermal background. Thus, while highly useful for probing conditions during the initial detonation and combustion of the HE, emission spectroscopy is not well-suited to measure the persistent gases remaining after the fireball has cooled.

Standoff (open-path) absorption spectroscopy provides a method to measure persistent gases produced from ODs which is not limited to probing regions of high temperature. Standoff absorption spectroscopy

probes the spectrum of light absorbed by molecular gases along a measurement path through the atmosphere between a source and detector, usually with a retro-reflector placed at one end of the path. The ability to perform measurements along an integrated path relaxes the requirements for sensor placement to intercept plumes. For example, the open path may be oriented perpendicular to the prevailing wind direction to measure plumes as they cross the path, allowing measurements if wind conditions change. The path may be located either close to the OD to probe plume gases and their temporal variations near the source or may be located farther away to measure plume gases after mixing and dilution with the atmosphere.

Infrared spectroscopy probes the characteristic ro-vibrational transitions of molecules, with higher absorption cross-sections than in other spectral regions such as NIR. The MWIR spectral region is valuable for measurement of combustion gases while the LWIR spectral region (8-12 μm) can be used to detect a wide range of trace gases. Open-path FTIR (OP-FTIR) has been used extensively to detect combustion and trace gases emitted from biomass burning.[17,18] For measurement of gases in OD experiments, OP-FTIR was used to measure infrared absorption over a 50 m segment of the atmosphere located ~700 m downwind of a of 46 kg TNT detonation.[4] In these OP-FTIR experiments, CO was detected at concentrations ranging from 0.2-1.4 ppm but $CO_2$ was not detected reliably. OP-FTIR in the MWIR-LWIR is typically limited to probing optical paths of a few hundred meters due to the limited spectral radiance of blackbody sources, which also prevents measurement with simultaneous high speed and high spectral resolution. Nevertheless, the broad spectral coverage provided by FTIR allows potential measurement of hundreds of molecular gas species.

Broadly-tunable swept-wavelength external cavity quantum cascade lasers (swept-ECQCLs)[6,19] provide an alternative method for open-path spectroscopy of molecular gases. The swept-ECQCL source generates a narrow-linewidth infrared laser that is tuned over a large range (> 100 $cm^{-1}$) at high speeds (> 100 Hz). Time-resolved detection of the swept-ECQCL light is used to measure absorption spectra for multiple gases along the measurement path, and spectral fitting produces time-resolved column densities or concentrations (mixing ratios) of the detected gases. The coherent laser source allows propagation over large distances through the atmosphere, which is essential for measurements in OD experiments to locate instruments and personnel outside the blast zone.

A LWIR swept-ECQCL source was recently used to perform standoff detection with a 235 m open path of multiple gas-phase molecular species in transient chemical plumes.[20] In these standoff measurements, the high wavelength tuning rate of the swept-ECQCL was shown to reduce measurement noise and improve detection sensitivity for trace gases in the presence of turbulent conditions along the measurement path.[20,21] Swept-ECQCL spectroscopy has also been previously used to measure combustion gases produced from HE detonations; in these experiments, a MWIR swept-ECQCL was propagated over a ~1 m path through an enclosed blast chamber and showed time-resolved detection of combustion gases CO, $CO_2$, $H_2O$, and $N_2O$ throughout the detonation, including their persistent concentrations after detonation.[22]

In this manuscript, we use a MWIR swept-ECQCL source to perform time-resolved standoff measurements of combustion gases CO, $CO_2$, $H_2O$, and $N_2O$ in a plume generated from an HE OD experiment. The MWIR swept-ECQCL system was located at a standoff distance of 830 m from a 41 kg charge of LX-14 (an HMX-based polymer-bonded high explosive) and was used to measure the infrared transmission through the post-detonation plume as it propagated through the beam path. The measurement path passed directly over the HE charge at a height of 15 m to measure gas concentrations near the post-detonation plume source. MWIR spectra were acquired continuously at 200 Hz to mitigate atmospheric turbulence and then averaged to 20 Hz to reduce noise. Absorbance spectra showed strong

variations as the HE post-detonation plume propagated through the measurement path. Spectral fits were used to determine the time-resolved changes in column density of CO, $CO_2$, $H_2O$, $N_2O$, and also the broadband attenuation from particulates. The swept-ECQCL measurements were compared to visible imaging/video data to correlate timing events and estimate plume dimensions. Emission factors (EFs) determined from analysis of the data are consistent with measurements performed on ODs using other techniques. Measurements acquired in the absence of the plume are used to characterize measurement sensitivity as a function of integration time. The results show that this new measurement technique is promising for standoff detection of multiple gases in plumes generated from OD or OB activities.

## II. EXPERIMENT

The MWIR swept-ECQCL was similar to systems used previously for laboratory measurements of combustion gases generated from HE detonations and biomass burning.[22,23] The swept-ECQCL was operated continuously to record broadband MWIR absorption spectra at a 200 Hz rate over a range from 2050-2230 $cm^{-1}$ (4.48-4.88 μm). Relative wavenumber calibration was performed by measuring fringes from a solid Si etalon with 0.416 mm thickness (free-spectral range 3.5 $cm^{-1}$) inserted temporarily into the beam path. Calibration of the absolute wavenumber was performed by comparing a measured transmission spectrum through the atmosphere with a reference spectrum of $CO_2$ and $H_2O$ simulated using HITRAN[24] under typical atmospheric conditions.

The MWIR swept-ECQCL was integrated into a standoff detection system which has been described in detail previously.[20] The previously-reported system used a LWIR swept-ECQCL, which was replaced by the MWIR swept-ECQCL. Other minor modifications included changing lenses to optimize anti-reflection coatings and changing the infrared detector for one with better responsivity in the MWIR (VIGO PVI-4TE-6). The output beam from the MWIR swept-ECQCL was expanded to a ~30 mm diameter ($1/e^2$) using a lens with focal length -20 mm and a gold-coated 90° off-axis parabolic mirror with 75 mm diameter and f=+230 mm. Return light was collected using an identical off-axis parabolic mirror and focused onto a TE-cooled HgCdZnTe (MCZT) detector optimized for MWIR operation (VIGO PVI-4TE-6). The average power of the ECQCL over the 200 Hz scan was 5 mW at the output of the system.

The measurements were performed at the Lawrence Livermore National Laboratory Site 300. Figure 1(a) shows an overhead view of the measurement configuration, overlaid on imagery from Google Earth. The blue line shows the measurement path. The swept-ECQCL standoff system was located on an observation tower at a distance of 830 m from the HE charge. The ECQCL beam was directed to a gold-coated hollow corner cube retro-reflector with 127 mm clear aperture placed on the top of a pyramid-shaped hill located at a distance of 900 m from the swept-ECQCL system, which returned the beam to the ECQCL position. Figure 1(b) shows a photograph of the swept-ECQCL and standoff detection optical system positioned on the observation tower, which was ~130 m higher in altitude than the retroreflector. Figure 1(c) shows a photograph of the HE detonation and the position of the retroreflector. The beam path passed ~15 m above the HE charge. The HE charge consisted of 41 kg (90 lbs) of LX-14 explosive (95% HMX - 1,3,5,7-Tetranitro-1,3,5,7-tetrazoctane, 5% plastic binders) placed 1 m above ground level. Correlation of timing signals for detonation and measurements was coarsely determined via pre-synchronization of clocks to within 0.5 s; higher-resolution timing correlation was determined from the measured data as discussed later. Prevailing winds near the HE charge obtained from on-site meteorological data were in the direction indicated in Fig. 1(a), with average speeds ~6 m/s at ground level and 11-12 m/s at heights > 10 m above ground level.

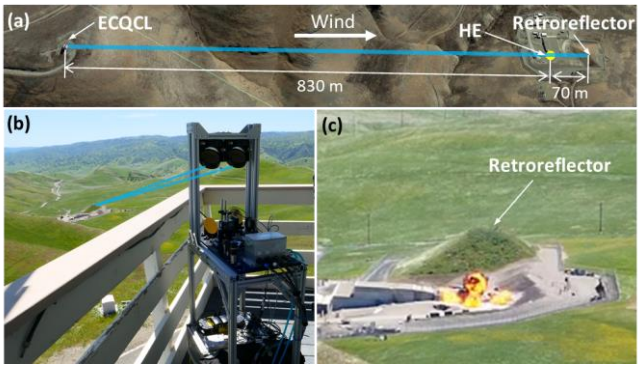


FIG. 1. Experimental details. (a) overhead view of measurement configuration from Google Earth. The blue line shows the measurement path between the swept-ECQCL and the retroreflector located 900 m away, and the position of the HE charge. (b) Photograph of swept-ECQCL standoff measurement system during measurements. (c) Photograph of HE detonation and retroreflector position.

## III. RESULTS

Video imagery at 30 frames per second (fps) was obtained from the vantage point of the swept-ECQCL system and captured the detonation and subsequent plume propagation. Figure 2 shows selected frames from the video at the times indicated. The scale bar in the photographs represents a 50 m distance on the ground at the location shown, based on imagery and distances in Google Earth. The approximate retroreflector position is indicated by the black square region of interest (ROI) in the figure. After detonation, a visible plume of dust and soot propagated upward and toward the retroreflector location, intersecting the ECQCL beam path at ~5 s. After 30 s, the plume had propagated past the retroreflector.

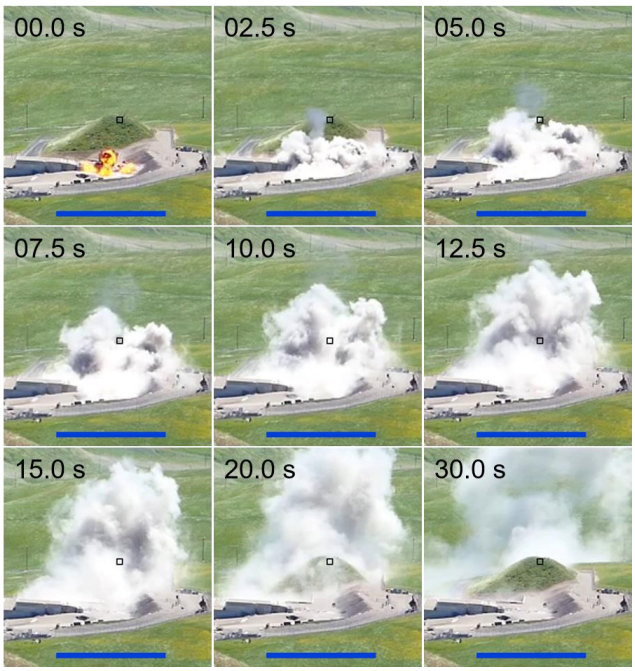


FIG. 2. Selected frames from video of HE detonation. Times listed are relative to detonation. The black square marks the retroreflector location and the ROI used for analysis of the video frames. The blue scale bar represents 50 m on the ground at the location shown.

Propagation through the 1800 m optical pathlength to and from the retroreflector resulted in strong absorption from atmospheric gases. Figure 3(a) shows the swept-ECQCL intensity versus wavenumber measured over the 1800 m path, recorded 300 s before the HE detonation. In this MWIR spectral region, strong absorption lines from $CO_2$, $H_2O$, and $N_2O$ are visible in the scan, along with weaker absorption lines from CO. To remove effects of the atmospheric absorption (which is mostly static over the time periods interrogated) and to highlight the changes in the spectrum produced by the HE detonation event, absorbance spectra were computed with respect to the background intensity $I_0(\nu)$ plotted in Fig. 3(a) via $A_j(\nu) = -\ln[I_j(\nu)/I_0(\nu)]$. The absorbance spectra computed in this manner provide differences relative to the time at which the background was measured, which is useful for detecting transient events such as chemical plumes.[20]

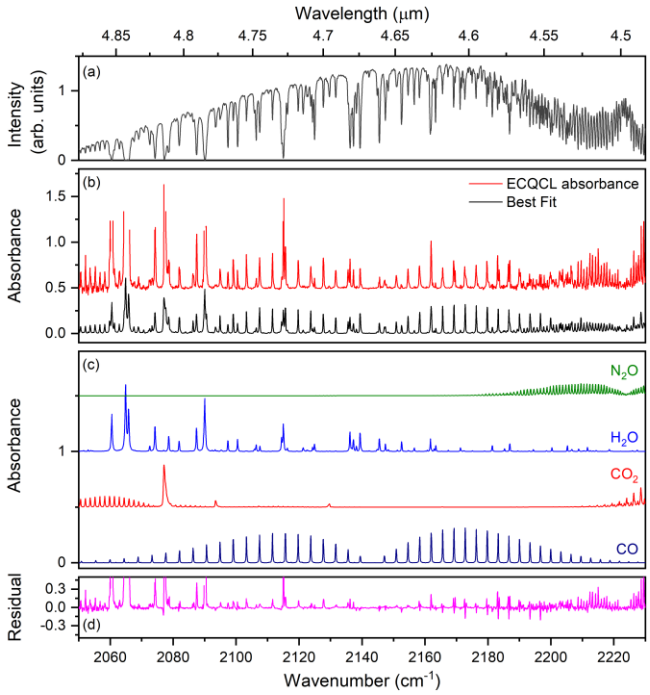


FIG.3. Spectral analysis. (a) Background intensity versus wavenumber (wavelength) from the swept-ECQCL scan measured by the detector after propagation over 1800 m pathlength through the atmosphere and 300 s before detonation (10 s average). (b) Measured absorbance relative to background (top) at 16.15 s after detonation (0.5 s average) and best fit spectrum (bottom). Spectra are offset for clarity. (c) Library reference spectra components used in spectral fit. Spectra are offset, from top to bottom: $N_2O$, $H_2O$, $CO_2$, and CO. (d) Fit residuals.

Measured absorbance spectra were fit using a linear weighted least squares (WLS) algorithm, which has been described previously.[6,20] Library absorption spectra for CO, $CO_2$, $H_2O$, and $N_2O$ were generated using HITRAN data[24], and convolved with a Gaussian function (0.2 $cm^{-1}$ full-width at half maximum) to account for an effective instrumental broadening. In addition to the library spectra for the four chemical species, a $7^{th}$ order polynomial baseline was included. The fit coefficients for each species were scaled for units of ppm*m and indicate the changes in column density relative to background levels before the detonation. The broadband (spectrally-flat) absorbance was obtained from the $0^{th}$ order polynomial fit component. The weighting function used in the WLS algorithm was $I_0(\nu)^2$. Spectral points with absorbance > 5 were not included in the fit, and only spectra with mean absorbance < 4 were fit. It was assumed that gas temperatures were 298 K and pressures were 1 atmosphere during the times at which the gas plume was measured. The reported column densities are derived from fits to path-integrated spectra

and thus represent an average plume column density assuming uniform physical conditions along the measurement path, and also represent the change in column density relative to background conditions (i.e. the average excess mixing ratios integrated over the measurement path).

Figure 3(b) shows an example absorbance spectrum obtained at 16.15 s after detonation (0.5 s average) when the plume was intersecting the beam path, along with the best fit spectrum determined by the WLS analysis. The polynomial baseline has been subtracted. Figure 3(c) shows the library spectra for the 4 combustion gases used in the fit with determined column densities CO=105 ppm*m, $CO_2$=82,000 ppm*m, $H_2O$=410,000 ppm*m, $N_2O$=24 ppm*m. Visual comparison of absorption lines in the experimental and library spectra confirms that all 4 gases are present in the plume and increased above the background levels. The agreement between experimental and fit spectrum is not perfect, and Fig. 3(d) shows the fit residual spectrum (weighted residual RMS=3.8E-3). High residuals are present near strong absorption peaks in Fig. 3(a), as expected due to the low light levels reaching the detector at these wavelengths from atmospheric attenuation. However, the WLS algorithm effectively ignores these strong absorption regions in the fit due to the weighting function $I_0(\nu)^2$, and instead the fit is preferentially performed to the weaker absorption peaks. The fit for $N_2O$ exhibits a residual structure suggesting small errors in wavelength calibration at this portion of the spectrum, or an incorrect approximation to instrumental broadening. Nevertheless, it is clear from the experimental spectrum in Fig. 3(b) that a net increase in absorption is observed corresponding to the $N_2O$ band.

Figure 4 shows various time-resolved quantities during the HE detonation event. Figure 4(a) shows time-dependence of the greyscale intensity in each video frame summed over the ROI (6x6 pixels). The frame immediately before the detonation was subtracted from all frames as a background. The greyscale intensity provides an overall timing context of the overlap of the visible plume with the ECQCL beam path. The greyscale intensity increases ~3 s after detonation as the plume (with a higher greyscale intensity than the background) enters the ROI. Variations in greyscale intensity are observed from 10-15 s due to variations in lighter/darker portions of the visible plume. At ~25 s after detonation, the visible plume has propagated downwind and no longer shows a significant overlap with the ROI.

Figure 4(b) plots the measured spectrally-integrated power of the swept-ECQCL transmitted through the plume as a function of time, which shows a good correlation in time with the visible imagery. In particular, during the initial rise in greyscale intensity as the plume enters the beam path, the detected ECQCL power decreases. From ~9-16 s, the detected power is below the noise floor of the system and the plume is effectively opaque to the MWIR light from the ECQCL. The opaque times from 9-16 s correlate with a decrease in greyscale intensity, reflecting a darker plume color possibly due to higher soot/dust contributions at these times. From 15-22 s, the power gradually increases and returns to its value before the detonation, correlating with the propagation of the visible plume downwind where it no longer intersects the ECQCL beam path.

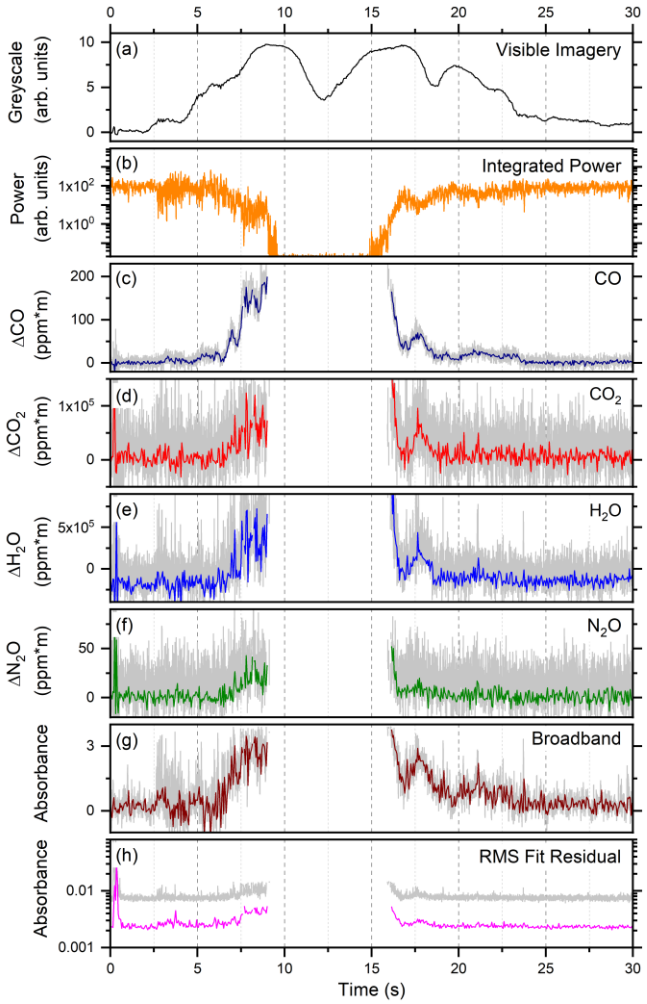


FIG. 4. Time-resolved measurements of HE detonation plume. (a) Greyscale intensity in retroreflector ROI. (b) Spectrally-integrated ECQCL power. (c) Change in CO column density. (d) Change in $CO_2$ column density. (e) Change in $H_2O$ column density. (f) Change in $N_2O$ column density. (g) Change in broadband absorbance spectral baseline. (h) RMS fit residual. In (c-h) light grey traces are for the 200 Hz measurement rate and colored traces are with averaging to 20 Hz.

Figures 4(c)-4(f) show results from the WLS analysis for the changes in column density of CO, $CO_2$, $H_2O$, and $N_2O$ in the plume following the HE detonation event. The lighter grey traces are results from analysis of the spectra as acquired at the 200 Hz rate, and the darker colored traces are results from analysis of spectra after averaging by 10× to a 20 Hz rate. The 4 gases show qualitatively similar behavior with increasing column density as the plume intersects the beam path from 3-8 s. The column densities could not be determined from 9-16 s due to the low levels of detected light transmitted through the opaque plume. From 16-23 s, the column densities decrease to background levels as the plume propagates past the retroreflector and no longer intercepts the measurement beam path. CO is detected with the highest signal-to-noise ratio (SNR), primarily due to the low background CO levels and high absorption cross-section. For $H_2O$ and $CO_2$, the high ambient levels (~10,000 ppm and ~400 ppm, respectively) over the 1800 m optical path length leads to high background absorption in the absence of the plume, as shown in Fig. 3(a), which in turn increases detection noise for these species. In addition, the WLS fitting de-weights spectral lines with high absorbance and instead uses lines with lower

absorption cross-section for fitting $CO_2$ and $H_2O$, with both effects leading to a reduced SNR. $N_2O$ has an atmospheric background of ~300 ppb, which also leads to significant absorption due to its high absorption cross-section as shown in Fig. 3(a). The negative offset to the $H_2O$ column density indicates a decrease in ambient concentration over the 300 s elapsed time between background and the HE plume detection, which is not unexpected due to local spatial/temporal variations in relative humidity.

The broadband absorbance plotted in Fig. 4(g) shows similar behavior to the other quantities and represents the spectrally-flat attenuation of the ECQCL beam from absorption or scattering due to particulates in the plume. In the case of the HE detonation, examples of particulates could be carbon soot, dust lofted from the ground, solid fragments liberated during the detonation, or condensed water droplets. Absorption from combustion gases in the plume are detected simultaneously with the broadband absorbance from particulates, as long as the broadband attenuation does not become so great that no MWIR light is transmitted through the plume. Attenuation at infrared wavelengths has been shown to be lower than at visible wavelengths in HE detonation fireballs,[25] and a similar relationship is expected for the post-detonation plume.

The weighted root-mean-squared (RMS) fit residuals are plotted in Fig. 4(h). The spectra averaged to 20 Hz provide residuals ~0.002 for most times, with sufficient temporal resolution to measure the dynamic changes as the plume propagates through the beam path. The fit residuals increase when the plume intercepts the beam path, as expected due to lower power levels on the detector and discrepancies between measured and fit spectra. A large increase in fit residuals is observed shortly after detonation at t=0.15 s, with a corresponding increased variation in nearly all parameters plotted in Fig. 4. As discussed next, this anomaly corresponds to an acoustic wave generated from the HE detonation passing the location of the retroreflector.

Although not easily discerned by eye in individual video frames, evidence of an acoustic (blast) wave was present in the analyzed video data as a disturbance to the grassy regions moving outward from the HE detonation. To better locate the acoustic wave front in the video frames, Fig. 5(a) shows images processed by taking the difference between successive frames and marking pixels in red where the greyscale intensity changed by more than 2.5%. The distance of the acoustic wave from the initial HE location versus time is shown in Fig. 5(b). The uncertainty in distance is estimated to be ±10% due to the video imaging geometry and resolution; nevertheless, the acoustic wave propagation is fit by a linear function with slope = 345±24 m/s, indicating an acoustic wave propagating at the speed of sound during these times and distances from the detonation, which is similar to prior observations.[26] A supersonic blast wave immediately after detonation could not be measured due to the limited time resolution of the video data. Based on the data shown in Fig. 5(b), the acoustic wave reaches the retroreflector distance of 70 m at t=0.15 s.

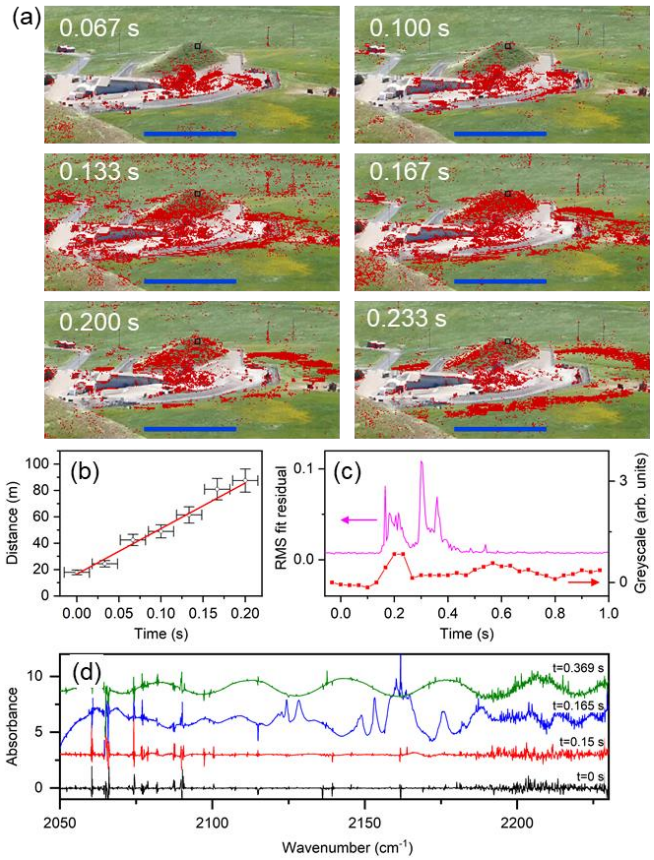


FIG. 5. Analysis of acoustic wave propagation. (a) Processed images from video. Red points show pixels where the greyscale intensity changed by more than 2.5% from the previous frame. The blue scale bar represents 50 m on the ground at the location shown. (b) Distance of acoustic wave propagation versus time using data from images. Solid line shows a linear fit with slope 345±24 m/s. (c) Registration of ECQCL data (RMS fit residuals) with acoustic wave arrival time at retroreflector. The acoustic wave arrival time at the retroreflector is visible by increased RMS fit residuals (magenta, left axis), which were set to coincide in time with acoustic wave arrival in the video data, obtained from the greyscale intensity in the ROI of the images (red, right axis). (d) Example absorbance spectra (baseline subtracted and offset for clarity) at indicated times before and during acoustic wave interaction with retroreflector.

Figure 5(c) shows the ECQCL RMS fit residuals and the video greyscale intensity in the ROI during the first second after detonation. The acoustic wave arrival at the retroreflector was evident in the ECQCL data as modulations in detected intensity over time scales shorter than a scan period. Figure 5(d) shows examples of ECQCL spectra recorded during these times. The spectra suggest that the acoustic wave caused the retroreflector to vibrate, leading to variations in the power returned to the detector. The initial interaction of the acoustic wave with the retroreflector leads to irregular variations in return power; however, after a short delay the oscillations became nearly sinusoidal. The oscillation frequency of the near-sinusoidal variation in return power shown in Fig. 5(d) at t=0.369 s is ~2 kHz, which is consistent with an acoustic/mechanical vibration frequency, likely due to the cushioned mounting used to provide shock-resistance to the retroreflector mirrors. Due to lack of an high-resolution absolute time standard for the ECQCL data to match the HE detonation, the detonation time (t=0) in the ECQCL data was located by setting the arrival of the acoustic wave to match the propagation time of t=0.15 s obtained from the video data.

## IV. Discussion

The measurement results demonstrate that combustion gases in the post-detonation plume are detected by the standoff swept-ECQCL measurement, and that large temporal variations in the column densities are observed. These temporal variations may arise from spatial inhomogeneities within the plume, and variations in the intersection of the plume with the measurement path. Due to the close proximity of the measurement path to the detonation, uniform spatial conditions along the measurement path cannot be assumed. Thus, given the path-integrated measurement it is not possible to determine excess mixing ratios (EMRs) solely from the ECQCL data. Quantities derived from relative mixing ratios, such as emission ratios (ERs),[27] or modified combustion efficiency (MCE)[27] may be calculated from the column densities assuming the gases are uniformly mixed at each point in the plume. However, for the measurements here the high noise in the $CO_2$ column density causes problems for calculating emission ratios relative to $CO_2$. Likewise, the high noise in the $CO_2$ measurement also creates problems for calculation of emission factors (EFs) using the carbon balance method,[2,27,28] which assumes all major products containing carbon can be measured accurately.

Therefore, to compare the ECQCL measurement results with other reported measurements of CO and $CO_2$ in plumes generated from HE detonations, we use an alternate approach by estimating the plume dimensions and overlap of the plume with the measurement path using additional video data. Figure 6 shows selected frames from video data acquired with a second camera located perpendicular to the measurement path. As visible in Fig. 6(a) at 0.25s after detonation, the initial plume consists of two components – a central darker component indicating soot from combustion, and a lighter component primarily due to dust lofted from the ground. These two components mix as they propagate downwind and overlap the ECQCL measurement path at different times. The variation in wind speed with distance above ground is apparent in the plume propagation, as is the disruption in plume propagation from the hill on which the retroreflector was located. The location of the plume front in the video images shown in Fig. 6 moves with a speed of ~7 m/s which is consistent with measured wind speeds near ground level.

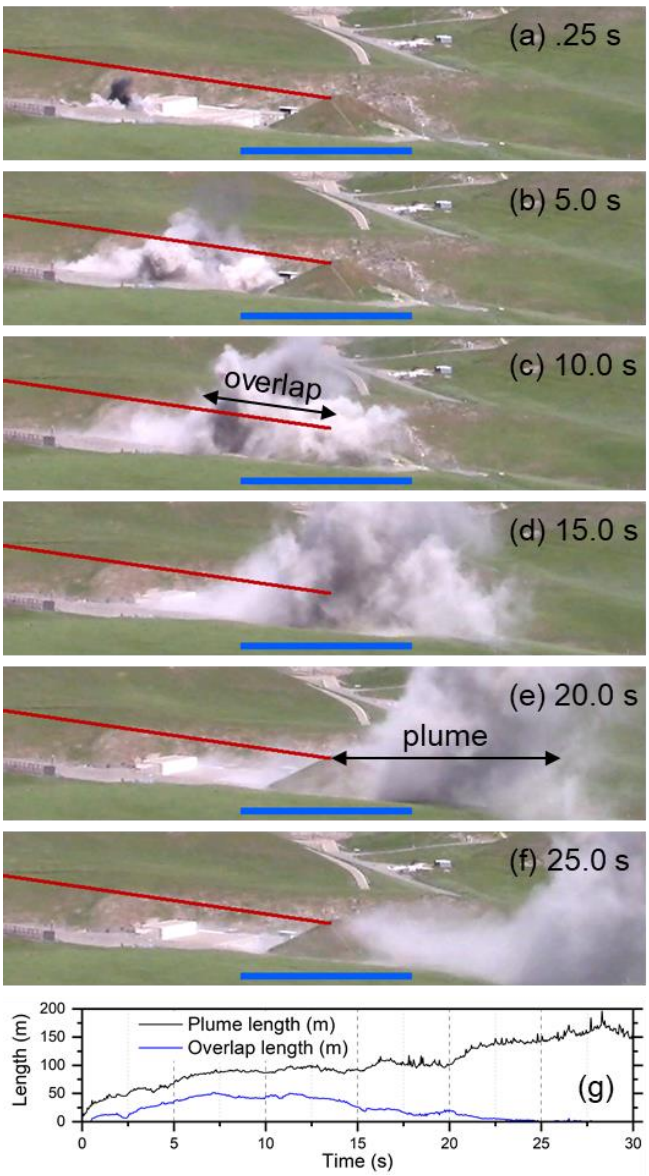


FIG. 6. Estimation of plume overlap with measurement path and plume length from video data obtained perpendicular to measurement path (red line). Video frames are shown for times after detonation (a) 0.25s, (b) 5s, (c) 10s, (d) 15s, (e) 20s, and (f) 25s. The blue scale bar represents 50 m on the ground at the location shown. (g) Plume length (black) and plume overlap length with measurement path (blue) as a function of time.

Video images were converted to greyscale intensity and the frame immediately before detonation was subtracted to create differential images. The greyscale intensity along the measurement path was plotted, and points with a change in greyscale intensity > 3× the background intensity were counted to estimate the length of the plume overlapping the measurement path. The total horizonal plume length (including regions outside the measurement path) was estimated similarly but using a horizonal line passing through the retroreflector position. Figure 6(g) shows the estimated plume overlap length with the measurement path and the total plume length. The estimated uncertainty of distances is ±10% based on uncertainty in the measurement scale calibration; however, the spatial inhomogeneity visible in the plume will lead to larger uncertainty in the actual overlap of the gas plume with the measurement path.

To estimate excess mixing ratios in the plume, the measured column densities were divided by 2× the plume overlap length; results are plotted in Fig. 7(a) for CO and Fig. 7(b) for $CO_2$. It should be stressed that the reported mixing ratios are estimates because the plume was not uniform along the measurement path, and the actual length of overlap of the gaseous components of the plume may not be the same as the overlap length determined from the video data (which includes dust lofted from the ground). Despite these uncertainties, it is still possible to compare qualitatively the various gas concentrations with each other and with other measurements. The measured CO concentrations ranged from 0-4 ppm, while the measured concentrations for $CO_2$ ranged from 0-3,500 ppm. Measured concentrations for $H_2O$ and $N_2O$ ranged from 0-20,000 ppm and 0-1 ppm, respectively (not shown in figure).

EFs of the gases were calculated by multiplying the gas mixing ratios by an approximate plume volume to estimate the total mass of each gas in the plume, relative to the initial HE mass of 41 kg. The plume volume versus time was estimated by a spherical volume with diameter shown in Fig. 6(g). As noted previously, the results have high uncertainty due to the rough estimates of plume size and approximations of uniform gas concentrations within the plume. Furthermore, the time variations of the measured concentrations resulted in a time-varying measured EF, which also contributes to a high uncertainty. Nevertheless, the average EFs estimated over a relatively stable time period between 7-9 s after detonation were CO=15±6 g/kg, $CO_2$=10,000±6,000 g/kg, and $N_2O$=3±2 g/kg. Figure 7(c) also shows the MCE calculated via $MCE = \Delta CO_2/[\Delta CO_2 + \Delta CO]$ and using the time-varying mixing ratios estimated by the ECQCL measurements. Based on the results, the MCE was >99%, indicating nearly complete combustion conditions in the detonation and post-detonation combustion (afterburn).

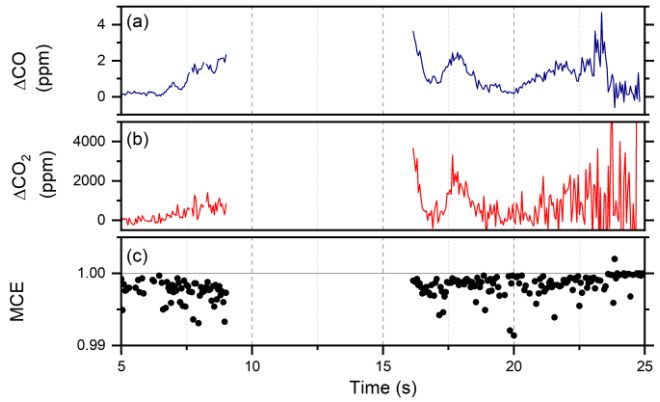


FIG. 7. Estimated excess mixing ratios for (a) CO and (b) $CO_2$ in plume based on plume overlap lengths obtained from analysis of visible video imagery. (c) Modified combustion efficiency (MCE) determined from measured CO and $CO_2$.

Previous measurements used a similar MWIR swept-ECQCL system to determine combustion gases generated from smaller 14 g charges detonated in an enclosed chamber with 2.5 $m^3$ volume.[22] For PBXN-5, which has a similar composition to LX-14, post-detonation gas concentrations were reported to be CO ~ 250 ppm, $CO_2$ ~ 3000 ppm, $H_2O$ ~ 400 ppm, and $N_2O$ ~ 14 ppm. Calculated EFs based on this data for PBXN-5 were CO~50 g/kg, $CO_2$~1,000 g/kg, and N2O~5 g/kg, with a corresponding MCE~92%. The lower CO and higher $CO_2$ concentrations for the larger outdoor LX-14 detonation relative to the smaller enclosed PBXN-5 detonation indicate a higher combustion efficiency, consistent with the increased oxygen available for afterburn in the outdoor conditions versus the enclosed chamber.

Table I provides a comparison of the ECQCL results with a selection of EFs and MCEs reported in the literature for enclosed chamber and open detonations. The CO EF of 15 g/kg measured here is reasonable

compared with the range of other reported values. The measured $CO_2$ EF of 10,000 g/kg is higher than other reported values, but not unreasonable considering the high uncertainty in the measurement of $CO_2$. The measured MCE agrees well with reported values for open detonations, which are higher than reported for detonations in enclosed chambers. Table 1 also shows the values predicted by the CHEETAH thermochemical code for comparison.[29] Because the CHEETAH calculation does not include post-detonation combustion with ambient air, the CO EF is significantly higher and the $CO_2$ EF is significantly lower than reported values for ODs, which is also reflected in the low MCE for the CHEETAH predictions.

TABLE I. Comparison of standoff ECQCL measurement results for emission factors (EF) and modified combustion efficiency (MCE) to reported literature values. Abbreviations in type column are OD (open detonation), EC (enclosed chamber), OB (open burn), and NC (no combustion).

| **Explosive** | **Mass (g)** | **CO EF (g/kg)** | **$CO_2$ EF (g/kg)** | **MCE (%)** | **Type** | **Source** |
|---|---|---|---|---|---|---|
| **LX-14 (95% HMX)** | 41,000 | 15±6 | 10,000±6,000 | 99.6±0.8 | OD | This study |
| **PBXN-5 (95% HMX)** | 14 | 50 | 1,000 | 92 | EC | [22] |
| **TNT** | 660 | 17 | 1,314 | 98 | EC | [2] |
| **TNT** | 230 | 10 | 1,500 | 99.3 | OD | [5] |
| **TNT** | 230 | 6.7 | 1,400 | 99.5 | OD | [5] |
| **RDX (claymore mine)** | 229 | 30 | 5,000 | 99.4 | OD | [5] |
| **Comp B (61% RDX, 39% TNT)** | 235 | 4.2 | 1,100 | 99.6 | OD | [5] |
| **Detonation train (62% RDX, 38% PETN)** | 178 | 9.4 | 910 | 99.0 | OD | [5] |
| **PBXN-110 (88% HMX)** | 1064 | 1.2 | 1,000 | 99.9 | OB | [5] |
| **LX-14 (95% HMX)** | | 96 | 278 | 74 | NC | CHEETAH |

Measurement noise was characterized by examining data obtained in the absence of the HE detonation event. Figure 8(a)-8(e) shows the time dependence of measurement results obtained starting 10 minutes after the HE detonation, plotted over a 500 s duration. Variations in detected power (spectrally-integrated) shown in Fig. 8(a) are observed due to turbulence-induced beam steering and indicate an intensity scintillation index[30] $\sigma_I = [\langle I^2 \rangle / \langle I \rangle^2 - 1]^{1/2}$ = 0.46 for the 200 Hz measurements. The measured scintillation index is ~3.5× higher than the value $\sigma_I = 0.13$ measured for previous standoff detection with a 235 m standoff distance using a LWIR swept-ECQCL,[20] which is expected given the larger standoff distance in the measurements reported here as well as differences in atmospheric conditions.

Fig. 6(b)-(e) show changes in column densities determined from WLS fits to the absorbance spectra with averaging to 20 Hz. With the exception of $H_2O$, the column densities for the gas species are nearly constant over the measurement period. For CO, $CO_2$, and $N_2O$, the presence of zero offset in column density further indicates the atmospheric concentrations have not changed significantly relative to the background measured 15 minutes earlier. The variations in $H_2O$ column density corresponds to a change of ~300 ppm concentration over the full measurement path, indicating a 3% change in relative humidity at a $H_2O$ background concentration of 10,000 ppm, which is not surprising given spatial and temporal variability in humidity.

Figure 8(f) shows results of an Allan-Werle analysis[31] of the output column densities. To calculate the Allan-Werle deviation, a data set of 60 s duration with measurements at 200 Hz (12,000 points) was used

for averaging times up to 1 s, and a data set of 600 s duration with averaged measurements at 20 Hz was used for averaging times 1-100 s. The left axis of Fig. 8(f) shows the Allan deviation in units of column density and provides the sensitivity for detection of transient plumes at various time scales of integration expressed as a noise-equivalent column density (NECD). The right axis of Fig. 8(f) shows the Allan deviation expressed as noise-equivalent concentration (NEC) in ppm for detection of changes in average concentration over the full 1800 m measurement path. Improved NECD for detection of CO, $CO_2$, and $N_2O$ is observed up to averaging times of 20 s. For $H_2O$, the variations in atmospheric concentration cause the Allan deviation to increase after 1 s averaging. It is possible that small local variations in CO, $CO_2$, and $N_2O$ concentrations also cause the increases in Allan deviation after 20 s; however, it is not possible to differentiate this possibility from instrumental drifts occurring over similar time scales.

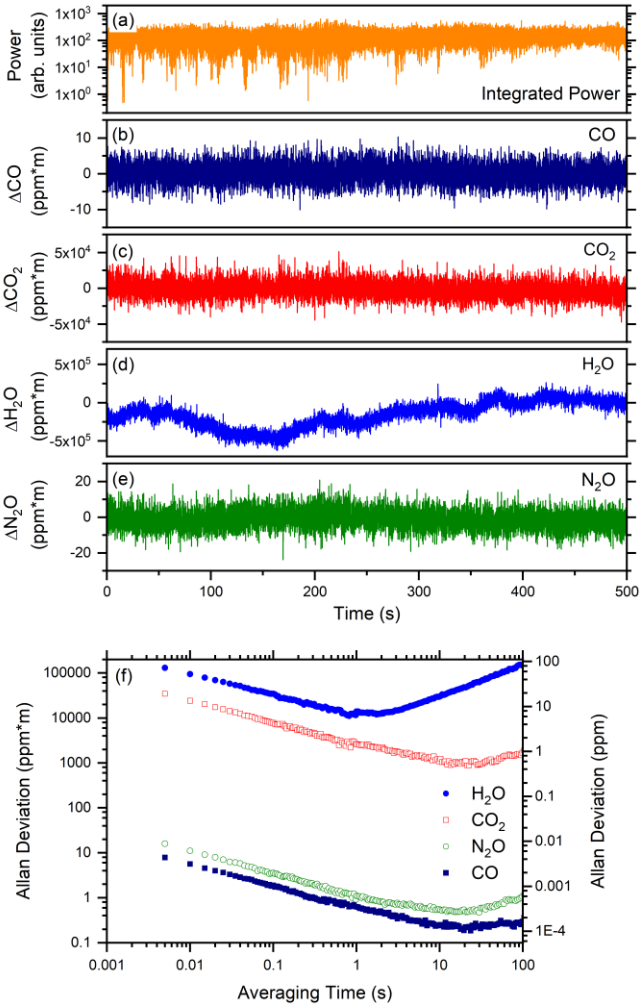


FIG. 8. Analysis of results measured 10 minutes after detonation with no plume present. (a) Spectrally-integrated ECQCL power. (b) Change in CO column density. (c) Change in $CO_2$ column density. (d) Change in $H_2O$ column density. (e) Change in $N_2O$ column density. (f) Allan deviation in units of column density (left axis) and units of ppm (right axis) for average concentrations over the full measurement path of 1800 m.

The Allan deviation analysis highlights the large difference in sensitivity for detection of CO and $N_2O$ with low atmospheric concentrations versus $CO_2$ and $H_2O$. Propagation over the 1800 m measurement path leads to increased noise relative to indoor measurements over shorter paths. For example, the 1 s

NECD values reported here are ~10× higher for CO and ~400× higher for $CO_2$ than for results using a similar MWIR swept-ECQCL for measurements of biomass burning over a 2.6 m path.[23] Detection of $CO_2$ in particular is hindered by the large absorption over long atmospheric paths, and improving NECD may require selection of different absorption bands to optimize the SNR. A shorter total measurement path would reduce the absorption contribution from ambient species, thereby improving the SNR for detection of changes due to the same species in the plume. However, benefits of detection over large atmospheric paths can be realized for species filling the entire path. For example, the results in Fig. 8(f) indicate that for measurements over an open atmospheric path length of 1800 m with 10 s averaging, NECs are CO~100 ppt, $N_2O$~300 ppt, and $CO_2$~600 ppb, which would provide a sensitive measurement of slower changes in these atmospheric gases.

The differential absorbance method used here was used to provide column densities based on the excess mixing ratios directly, and thus absolute column densities and mixing ratios were not determined. In principle, it should be possible to determine absolute column densities based on analysis and fitting of the background spectrum itself; however, an accurate reference measurement would be required for the intensity spectrum before propagation through the atmosphere. This could be performed using a second detector or by referencing the long-path measurement to a second shorter-path measurements. In practice, small variations in detector spectral responsivity or small changes in measurement configurations often prevent acquisition of an accurate reference spectrum to calculate the absolute absorbance without introducing other systematic errors. One advantage of the differential absorbance method used here is that a single detector is used in an identical geometry for the signal and background measurements.

## V. SUMMARY AND CONCLUSIONS

The measurements reported here provide an initial demonstration using a swept-ECQCL to perform standoff detection of combustion gases in a plume generated by a large-scale outdoor HE detonation. The swept-ECQCL was operated continuously to record broadband MWIR absorption spectra at a 200 Hz rate over a range from 2050-2230 $cm^{-1}$ (4.48-4.88 μm). The swept-ECQCL was located at a distance of 830 m away from a 41 kg charge of LX-14, providing a safe distance between the detonation and equipment/operators. The system was used to measure the transmission through the post-detonation plume propagating through the beam path. Spectral fits were used to determine the time-resolved changes in column densities of CO, $CO_2$, $H_2O$, and $N_2O$ along with the broadband attenuation. Analysis of visible imagery was used to provide timing correlations and to estimate the plume size and its overlap with the measurement path.

The measurement geometry used in the experiments reported here was constrained by the site topography and limited locations available for placing the ECQCL instrumentation and retroreflector. Locating the measurement path directly above the HE detonation was beneficial for determining gas column densities in a concentrated plume near the source shortly after detonation; however, the high broadband attenuation resulted in a time period of high plume opacity when measurements could not be performed. Furthermore, the measurement configuration limited the measurement times to < 30 s before the plume propagated past the retroreflector. Nevertheless, determination of time-resolved column densities and estimates of gas concentrations in the plume near the source and before propagation over long distances may be extremely valuable as inputs to or validation measurements for plume transport models.

Future measurement configurations could include locating the entire measurement path downwind of the HE detonation, either parallel or perpendicular to the prevailing wind direction. In this case, spreading of

the plume in time and space during propagation could increase the duration over which it is detected and increase the interaction length of the plume with the measurement path. Longer plume propagation distances would also likely improve uniformity of species within the plume. In practice, a combination of sensing techniques would be most valuable for characterizing the post-detonation plume completely. For example, ruggedized optical absorption sensors placed near the source or even inside the fireball could measure $H_2O$ concentrations and temperatures at high speeds to determine source conditions,[32,33] and similar sensors may be applicable to other gases of interest. Point sensors or samplers based on swept-ECQCL[6] or other technologies[3] placed downwind of the detonation could provide high sensitivity time-resolved measurements of mixing ratios at discrete locations. Finally, open-path detection techniques can provide time-resolved measurements of column densities averaged over the plume, and multiple systems could be deployed to provide measurements at different distances from the source.

The MWIR swept-ECQCL system here provided measurement of 4 combustion-related gases, with the CO measurement providing the highest SNR. It is worth noting that $N_2O$ can be detected by the system at trace levels with high sensitivity. The addition of $N_2O$ detection to more commonly detected $NO_x$ species NO and $NO_2$ may provide new information on HE detonation and combustion efficiency. Use of a LWIR swept-ECQCL system[20] would allow extension of the measurement to many other trace gases of interest produced in HE detonations.[5] Finally, the standoff measurement is of course not limited to HE OD experiments but is a general technique applicable to other gas detection scenarios. Examples may include measurement of EFs from OB of military munitions, measurement of gases and EFs from biomass burning, characterization of gases emitted from factories or other facilities, and many others. Overall, the use of standoff open-path measurements with swept-ECQCL sources provides a powerful method of real-time characterization of the gas composition of plumes generated from HE detonations or other transient events.

## VI. Acknowledgements

This work was supported by the National Nuclear Security Administration, Defense Nuclear Nonproliferation R&D Office and the Department of Energy Phase I SBIR program [DE-SC0019855]. The Pacific Northwest National Laboratory is operated for the U.S. Department of Energy (DOE) by the Battelle Memorial Institute under Contract No. DE-AC05-76RL01830. This work was performed under the auspices of the U.S. Department of Energy by Lawrence Livermore National Laboratory under Contract DE-AC52-07NA27344. We thank the many researchers and staff at Lawrence Livermore National Laboratory Site 300 for conducting HE and site operations. The authors acknowledge important interdisciplinary collaboration with scientists and engineers from LANL, LLNL, MSTS, PNNL, and SNL. Authors Mark Phillips and Jeremy Yeak are an employee and owner, respectively, of a commercial entity Opticslah, LLC. LLNL-JRNL-811691

## VII. Data Availability

The data that support the findings of this study are available from the corresponding author upon reasonable request.

## VIII. References


[1] I. Zawadzka-Małota, Journal of Sustainable Mining **14,** 173 (2015).

[2] K. McNesby, M. Nusca, M. McQuaid, C.-C. Chen, R. Benjamin, R. Thompson, E. Summers, W. Sickels, R. Sparks, A. Holder, B. Gullett, and J. Aurell, "Report ARL-TR-8456: Development of Methodologies for Evaluating Emissions from Metal-Containing Explosives and Propellants," (2018).

[3] J. Aurell, B. K. Gullett, D. Tabor, R. K. Williams, W. Mitchell, and M. R. Kemme, Journal of Hazardous Materials **284,** 108 (2015).

[4] B. J. Kim, M. R. Kemme, B. Gullett, M. J. Rood, R. Hashmonay, W. Yuen, D. Johnsen, and S. Koloutsou-Vakakis, "SERDP Report WP-1672: Feasibility of New Technology to Comprehensively Characterize Air Emissions from Full Scale Open Burning and Open Detonation," (2010).

[5] W. J. Mitchell and J. C. Suggs, "Report EPA/600/R-98/103: Emission Factors for the Disposal of Energetic Materials by Open Burning and Open Detonation (OB/OD)," (1998).

[6] M. C. Phillips, M. S. Taubman, B. E. Bernacki, B. D. Cannon, R. D. Stahl, J. T. Schiffern, and T. L. Myers, Analyst **139,** 2047 (2014).

[7] W. K. Lewis, C. G. Rumchik, P. B. Broughton, and C. M. Lindsay, Journal of Applied Physics **111,** 014903 (2012).

[8] J. R. Carney, J. S. Miller, J. C. Gump, and G. I. Pangilinan, Review of Scientific Instruments **77,** 063103 (2006).

[9] J. D. Koch, S. Piecuch, J. M. Lightstone, J. R. Carney, and J. Hooper, Journal of Applied Physics **108,** 036101 (2010).

[10] N. Glumac, Shock Waves **23,** 131 (2013).

[11] L. Maiz, W. A. Trzcinski, and J. Paszula, Optics and Lasers in Engineering **88,** 111 (2017).

[12] J. M. Gordon, K. C. Gross, and G. P. Perram, Optical Engineering **53,** 021106 (2014).

[13] J. M. Gordon, K. C. Gross, and G. P. Perram, Proceedings of SPIE **7330,** 733006 (2009).

[14] K. C. Gross, J. Wayman, and G. P. Perram, Proceedings of the SPIE **6566,** 656613 (2007).

[15] K. C. Gross, G. P. Perram, and R. F. Tuttle, Proceedings of the SPIE **5811,** 100 (2005).

[16] J. A. Orson, W. F. Bagby, and G. P. Perram, Infrared Physics & Technology **44,** 101 (2003).

[17] S. K. Akagi, I. R. Burling, A. Mendoza, T. J. Johnson, M. Cameron, D. W. T. Griffith, C. Paton-Walsh, D. R. Weise, J. Reardon, and R. J. Yokelson, Atmospheric Chemistry and Physics **14,** 199 (2014).

[18] R. J. Yokelson, D. W. T. Griffith, and D. E. Ward, Journal of Geophysical Research-Atmospheres **101,** 21067 (1996).

[19] B. E. Brumfield, M. S. Taubman, J. D. Suter, and M. C. Phillips, Optics Express **23,** 25553 (2015).

[20] M. C. Phillips, B. E. Bernacki, S. S. Harilal, J. Yeak, and R. J. Jones, Optics Express **28,** 7408 (2020).

[21] M. C. Phillips and B. E. Brumfield, Optical Engineering **57,** 011003 (2018).

[22] M. Phillips, B. Bernacki, S. Harilal, B. Brumfield, J. Schwallier, and N. Glumac, Journal of Applied Physics **126,** 093102 (2019).

[23] M. C. Phillips, T. L. Myers, T. J. Johnon, and D. R. Weise, Optics Express **28,** 8680 (2020).

[24] I. E. Gordon, L. S. Rothman, C. Hill, R. V. Kochanov, Y. Tan, P. F. Bernath, M. Birk, V. Boudon, A. Campargue, K. V. Chance, B. J. Drouin, J. M. Flaud, R. R. Gamache, J. T. Hodges, D. Jacquemart, V. I. Perevalov, A. Perrin, K. P. Shine, M. A. H. Smith, J. Tennyson, G. C. Toon, H. Tran, V. G. Tyuterev, A. Barbe, A. G. Csaszar, V. M. Devi, T. Furtenbacher, J. J. Harrison, J. M. Hartmann, A. Jolly, T. J. Johnson, T. Karman, I. Kleiner, A. A. Kyuberis, J. Loos, O. M. Lyulin, S. T. Massie, S. N. Mikhailenko, N. Moazzen-Ahmadi, H. S. P. Muller, O. V. Naumenko, A. V. Nikitin, O. L. Polyansky, M. Rey, M. Rotger, S. W. Sharpe, K. Sung, E. Starikova, S. A. Tashkun, J. Vander Auwera, G. Wagner, J. Wilzewski, P. Wcislo, S. Yu, and E. J. Zak, Journal of Quantitative Spectroscopy & Radiative Transfer **203,** 3 (2017).

[25] R. Lodes, H. Krier, and N. Glumac, Propellants Explosives Pyrotechnics **45,** 406 (2020).

[26] J. M. Gordon, K. C. Gross, and G. P. Perram, Combustion Explosion and Shock Waves **49,** 450 (2013).

[27] I. R. Burling, R. J. Yokelson, D. W. T. Griffith, T. J. Johnson, P. Veres, J. M. Roberts, C. Warneke, S. P. Urbanski, J. Reardon, D. R. Weise, W. M. Hao, and J. de Gouw, Atmospheric Chemistry and Physics **10,** 11115 (2010).

[28] R. J. Yokelson, J. G. Goode, D. E. Ward, R. A. Susott, R. E. Babbitt, D. D. Wade, I. Bertschi, D. W. T. Griffith, and W. M. Hao, Journal of Geophysical Research-Atmospheres **104,** 30109 (1999).

[29] S. Bastea, L. E. Fried, W. M. Howard, I.-F. W. Kuo, P. C. Souers, and P. A. Vitello, "Cheetah 8.0."

[30] L. C. Andrews, R. L. Phillips, and C. Y. Hopen, *Laser Beam Scintillation with Applications* (SPIE Press, 2001).
[31] P. Werle, R. Mucke, and F. Slemr, Applied Physics B-Photophysics and Laser Chemistry **57,** 131 (1993).
[32] J. R. Carney, J. M. Lightstone, S. Piecuch, and J. D. Koch, Measurement Science and Technology **22,** 045601 (2011).
[33] C. Murzyn, A. Sims, H. Krier, and N. Glumac, Optics and Lasers in Engineering **110,** 186 (2018).